Human Molecular Genetics, 2010, Vol. 19, No. 20 ***4059–4071***
doi:10.1093/hmg/ddq329
Advance Access published on August 9, 2010

Cardiac defects contribute to the pathology of spinal muscular atrophy models

Monir Shababi[1,*,†], Javad Habibi[2,†], Hsiao T. Yang[3], Spencer M. Vale[1], Will A. Sewell[1] and Christian L. Lorson[1,*]

[1]Department of Veterinary Pathobiology, Bond Life Sciences Center, [2]Department of Internal Medicine, School of Medicine, University of Missouri and [3]Department of Biomedical Sciences, University of Missouri, Columbia, MO, USA

Received June 3, 2010; Revised July 13, 2010; Accepted July 30, 2010

Spinal muscular atrophy (SMA) is an autosomal recessive disorder, which is the leading genetic cause of infantile death. SMA is the most common inherited motor neuron disease and occurs in approximately 1:6000 live births. The gene responsible for SMA is called *Survival Motor Neuron-1* (*SMN1*). Interestingly, a human-specific copy gene is present on the same region of chromosome 5q, called SMN2. Motor neurons are the primary tissue affected in SMA. Although it is clear that SMA is a neurodegenerative disease, there are clinical reports that suggest that other tissues contribute to the overall phenotype, especially in the most severe forms of the disease. In severe SMA cases, a growing number of congenital heart defects have been identified upon autopsy. The most common defect is a developmental defect referred to as hypoplastic left heart. The purpose of this report is to determine whether cardiac tissue is altered in SMA models and whether this could contribute to SMA pathogenesis. Here we identified early-stage developmental defects in a severe model of SMA. Additionally, pathological responses including fibrosis and oxidative stress markers were observed shortly after birth in a less severe model of disease. Similarly, functional differences were detected between wild-type and early-stage SMA animals. Collectively, this work demonstrates the importance of cardiac development and function in these severe models of SMA.

INTRODUCTION

Spinal muscular atrophy (SMA) is an autosomal recessive disorder, which is the leading genetic cause of infantile death (1). SMA is the most common inherited motor neuron disease and occurs in approximately 1:6000 live births (1,2). SMA results from homozygous loss of a gene called *Survival Motor Neuron-1* (*SMN1*) (3). Humans express a copy gene, SMN2, from the same region of chromosome 5q as a result of duplication and inversion. SMN2 is nearly identical to SMN1 (3,4); however, mutations in *SMN2* have no clinical consequence if intact SMN1 is present. The reason that *SMN2* cannot fully complement the SMN1 deficiency is that the majority of *SMN2*-derived transcripts are alternatively spliced (5–7), leading to a truncated and unstable protein that lacks the 16 amino acids encoded by SMN exon 7 (normally the last coding exon) (3,5,8–11).

SMA is caused by reduced levels of SMN, which results in a loss of functional motor neurons. SMN, however, is ubiquitously expressed and performs an essential function in all tissues that relates to global gene expression: snRNP biogenesis (12). Briefly, SMN catalyzes the formation of the building blocks for the splicing machinery within the cytoplasm, forming Sm protein/snRNA complexes that are then translocated into the nucleus for splicing (12). There is still considerable debate over whether disruption of this critical cellular function accounts for SMA development. Importantly, however, it is clear that SMA is caused by low levels of SMN, not by the elimination of all SMN since complete loss of SMN is embryonic lethal. Consistent with this, Cre-lox models have been developed in which full-length SMN is completely ablated in specific tissues including skeletal muscle or cardiac tissue, leading to dramatic tissue-specific defects that are not consistent with a typical SMA phenotype (13,14).

*To whom correspondence should be addressed at: Department of Veterinary Pathobiology, Life Sciences Center, University of Missouri, Room 471G, Columbia, MO 65211, USA. Tel: +1 5738842219; Fax: +1 5738849395; Email: lorsonc@missouri.edu (C.L.L.), shababim@missouri.edu (M.S.)
†These authors contributed equally to this work.

Based on our current knowledge of SMA, motor neurons are the primary tissue affected in SMA. Although it is clear that SMA is a neurodegenerative disease, there are clinical reports suggesting that other tissues contribute to the overall phenotype, especially in the most severe forms of the disease. Upon autopsy, a growing number of congenital heart defects have been recognized, including atrial septal defects, dilated right ventricle (RV) and ventricular septal defects (15). The most common defect is a developmental defect referred to as hypoplastic left heart syndrome (15). Our goal is to examine the role of SMN in cardiac development and the impact of heart defects in SMA pathogenesis. As SMA therapeutics and supportive measures are further developed, it will be essential to fully understand the role of SMN in cardiac development and to determine whether additional tissues are at risk in SMA patients other than motor neurons. We investigated the requirement for Smn in cardiac development and contribution of the heart impairments to the SMA phenotype by examining the heart at different developmental stages starting from embryos in a severe model ($Smn^{-/-}$, $SMN2^{+/+}$) and thereafter at different time points post-birth in a well-established model of SMA, the SMAΔ7 model ($Smn^{-/-}$, $SMN2^{+/+}$; SMN$\Delta7^{+/+}$). Our histology results indicate that cardiac remodeling initiates at the embryonic stage in the severe model, although motor neurons are not yet visibly affected at this stage. We also observed similar structural defects initiating post-birth in the heart of SMAΔ7 mice as well as increasing levels of interstitial fibrosis as age progresses. Our results suggest that oxidative stress, which is the underlying mechanism of cardiac fibrosis, initiates at the time of disease onset and develops significantly in the following days. Furthermore, our results with functional analysis demonstrate physiological defects such as drastically reduced heart rate in SMA mice.

RESULTS

Remodeling of inter-ventricular septum and left ventricular wall in embryos of severe model

The severe model of SMA lacks murine Smn and contains two copies of human SMN2 ($Smn^{-/-}$, $SMN2^{+/+}$). The severity of this model results in early death 4–5 days post-birth (16,17). During the development of the severe SMA colony, we noticed that the severe SMA animals were frequently at lower numbers at birth than would be predicted by Mendelian genetics (~25%), whereas SMA embryos were present in expected ratios early during development (data not shown). Though motor neurons are fundamental, very severe reductions in motor neurons do not necessarily lead to embryonic lethality, rather death occurs shortly after birth. Therefore, we speculated that a critical organ system, such as the heart, was impacted by very low levels of SMN. Initially, we decided to analyze the structural integrity of the embryonic SMA heart from severe SMA mice. One of the most important structural determinants in the heart is septal and ventricular morphology. In humans, ventricular septal defect such as reduced width of the inter-ventricular septum (IVS) is most intimately related to the narrowing immediately underneath the aortic valve (18). In addition, obstruction at the middle region of the left ventricular outflow tract is largely caused by reduced width of the IVS (18). To determine whether any abnormalities in IVS were present, we evaluated the septum morphology in severe and wild-type embryos at e17.5. Interestingly, our bright-field image analysis of VVG (Verhoeff–van Gieson)-stained cross-sections of embryonic heart demonstrated a significant reduction in the width of IVS in embryonic SMA heart compared with wild-type ($P = 0.007$) (Fig. 1). We compared the depth of the left ventricular wall in the embryonic severe heart with that in wild-type embryonic hearts. The wall of the left ventricle (LV) is thicker than the RV to enable the LV to pump blood more forcefully to the rest of the body. Our results demonstrate a thin and branched left ventricular wall in severe embryonic SMA hearts compared with a thick and well-developed left ventricular wall in wild-type ($P = 0.05$) (Fig. 2).

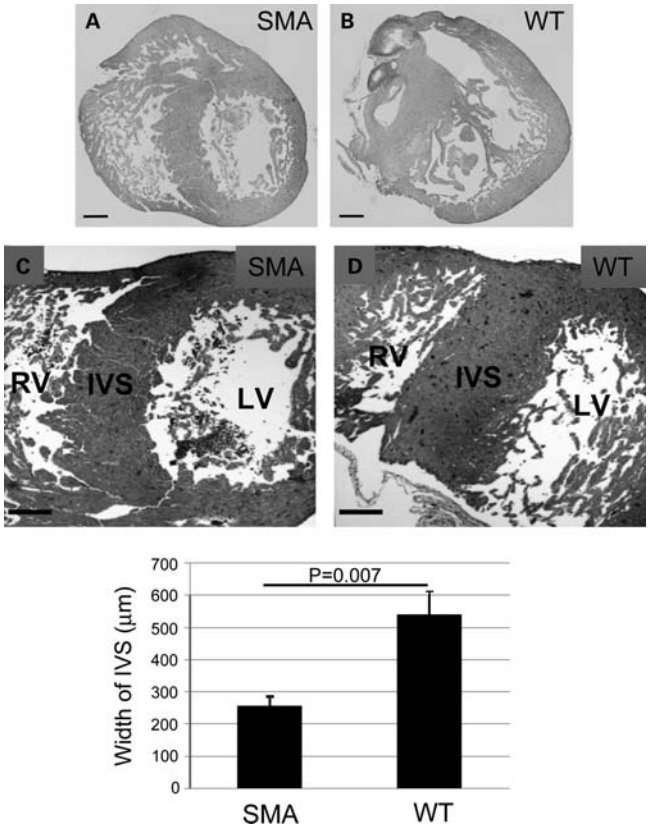

Figure 1. IVS remodeling occurs at the embryonic stage in an SMA severe model. Representative bright-field images of 4 μm VVG-stained cross-sections of embryonic heart in SMA severe model ($Smn^{-/-}$, $SMN2^{+/+}$) (**A** and **C**) and wild-type ($Smn^{+/+}$, $SMN2^{+/+}$) (**B** and **D**). VVG stains elastin (black), nuclei (blue black), collagen type III (pink) and connective tissue (yellow). (A and B) Intact heart cross-sections are shown. (C and D) IVS with part of right and LVs is shown. Morphometric analysis was applied to 4× images to measure the width of the IVS. The error bars present ± SE. *P*-value was determined by two-tailed *t*-test ($P = 0.007$). IVS, inter-ventricular septum; LV, left ventricle; RV, right ventricle. WT, $n = 4$; SMA, $n = 4$. Scale bar: 200 μm.

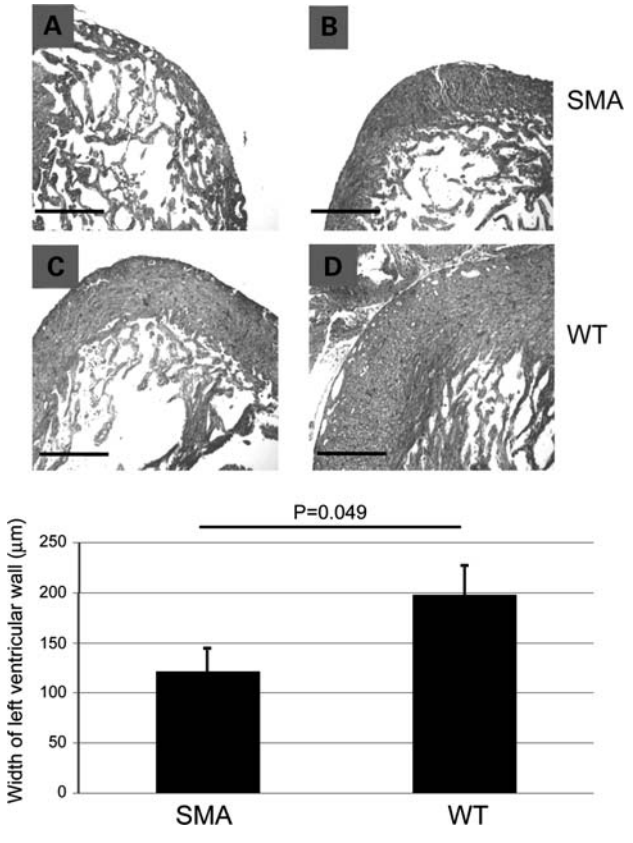

Figure 2. Left ventricular wall remodeling occurs at the embryonic stage in an SMA severe model. Representative bright-field images of 4 μm VVG-stained cross-sections indicating left ventricular wall of embryonic heart of SMA severe model ($Smn^{-/-}$, $SMN2^{+/+}$) (**A** and **B**) and wild-type ($Smn^{+/+}$, $SMN2^{+/+}$) (**C** and **D**). Morphometric analysis was applied to 10× images to measure the width of the left ventricular wall. The error bars present ±SE. *P*-value was determined by two-tailed *t*-test ($P < 0.05$). WT, $n = 4$; SMA, $n = 4$. Scale bar: 200 μm.

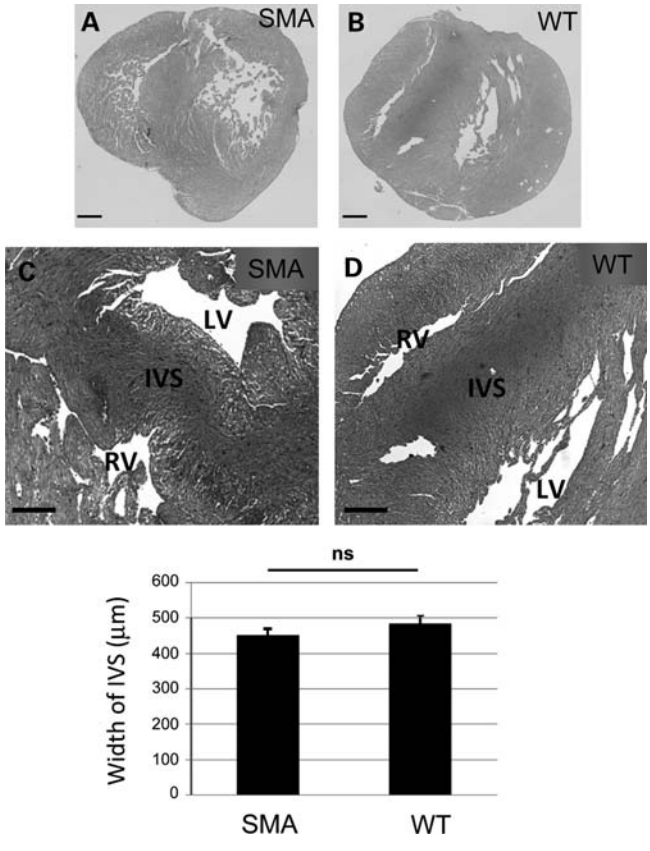

Figure 3. IVS remodeling is not evident in 2-day-old hearts of SMAΔ7 mice. Representative bright-field images of 4 μm VVG-stained cross-sections of 2-day-old SMAΔ7 ($mSmn^{-/-}$, $SMN^{+/+}$, $SMNΔ7^{+/+}$) (**A** and **C**) and wild-type ($mSmn^{+/+}$, $SMN^{+/+}$, $SMNΔ7^{+/+}$) (**B** and **D**) hearts. (A and B) Intact heart cross-sections are shown. (C and D) IVS with part of right and LVs is shown. Morphometric analysis was applied to 4× images to measure the width of the IVS. The error bars present ±SE. *P*-value was determined by two-tailed *t*-test ($P > 0.05$). IVS, inter-ventricular septum; LV, left ventricle; RV, right ventricle. WT, $n = 4$; SMA, $n = 4$. Scale bar: 200 μm.

IVS remodeling in SMAΔ7 mouse model

Even though the congenital heart defects have been reported in severe forms of SMA, we were interested to analyze the heart abnormalities in the SMAΔ7 mouse model as well, since this is a commonly used model in the field for biological and translational studies. The genotype of SMAΔ7 mice is identical to the severe model except for the addition of SMNΔ7 cDNA that lessens the disease severity. This model still demonstrates a severe phenotype with disease onset at 7–10 days and a modestly extended life span (13–18 days) compared with the severe model (4–6 days). To detect any cardiac remodeling at different developmental stages, we chose to examine the hearts of SMAΔ7 mice at several neonatal time points: P2, P5 and P9. We chose early time points (P2 and P5) to uncover any structural deformity that may occur early in life and a late time point (P9) to determine the effect of SMN deficiency on the progression of heart damage that may eventually lead to heart failure. Bright-field image analysis of VVG-stained cross-sections of the heart harvested at P2 demonstrated that the width of IVS in SMAΔ7 mice and the wild-type littermates is similar, indicating that the structural defects observed in the more severe model are not present at this stage and presumably at embryonic stages (Fig. 3). However, we observed a considerable reduction in the width of IVS in the heart of P5 SMA mice compared with age-matched wild-type ($P = 0.01$) (Fig. 4). Similarly, the width of the IVS in SMAΔ7 mice was significantly different compared with wild-type at P9 ($P = 0.01$) (Fig. 5). Morphological observations of IVS images also revealed partial flattening of the IVS in the SMA heart harvested at P5 but were more pronounced at P9 (Figs 4 and 5). The normal geometry of the IVS in wild-type mice involves a curve-shaped surface which is essential for balancing the pressure difference between the LV and the RV. The IVS of SMA heart lacks the normal curvature which results in a D-shaped LV.

One of the factors that may contribute to a thin septum is a developmental delay or a difference in heart size. To determine whether SMA mice have abnormally sized hearts, we measured the ratio of the heart weight to the total body weight of SMAΔ7 and wild-type mice at each of the previously examined time points (P2, P5, P9). Our analysis indicated a very similar ratio of the heart to body mass in both animals, confirming that the reduced size of the SMA heart is due to the small body mass rather than irregular loss of growth in the heart (Fig. 6). In addition, examining the heart cross-sections which were

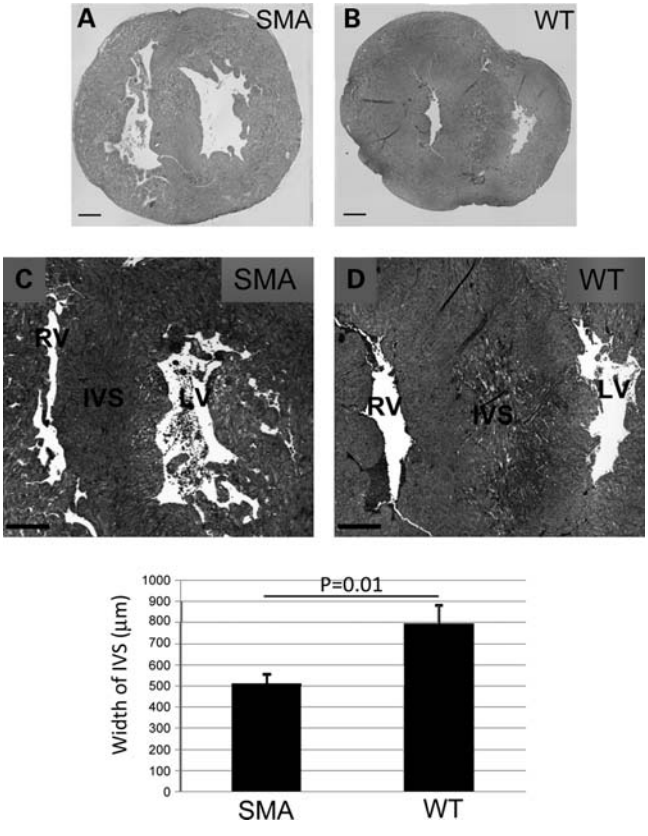

Figure 4. IVS remodeling is visible in 5-day-old hearts of SMAΔ7 mice. Representative bright-field images of 4 μm VVG-stained cross-sections of 5-day-old SMAΔ7 (**A** and **C**) and wild-type (**B** and **D**) hearts. (A and B) Intact heart cross-sections are shown. (C and D) IVS with part of right and LVs is shown. Morphometric analysis was applied to 4× images to measure the width of the IVS. The error bars present ±SE. *P*-value was determined by two-tailed *t*-test ($P = 0.01$). IVS, inter-ventricular septum; LV, left ventricle; RV, right ventricle. WT, $n = 4$; SMA, $n = 4$. Scale bar: 200 μm.

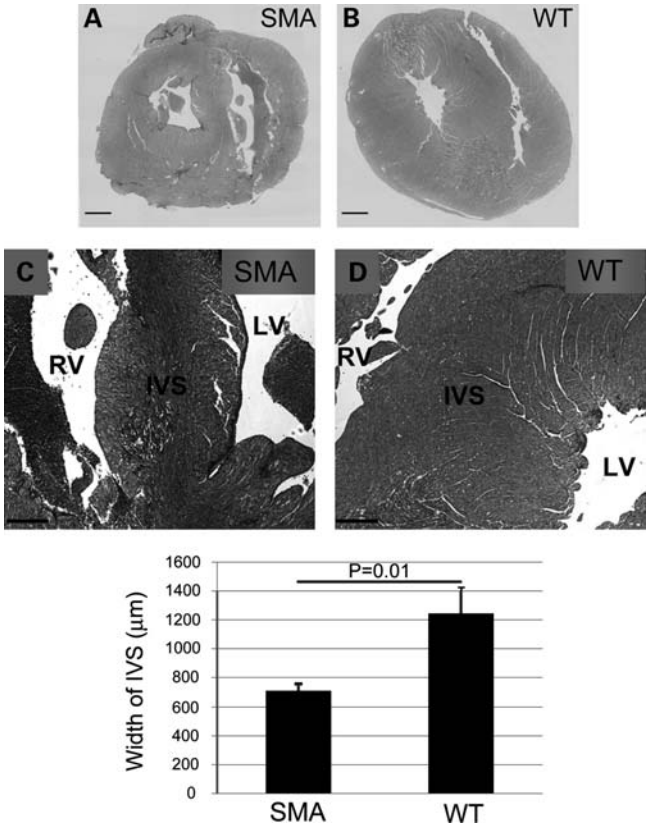

Figure 5. IVS thinning is well advanced to 9-day-old hearts of SMAΔ7 mice. Representative bright-field images of 4 μm VVG-stained cross-sections of 9-day-old SMAΔ7 (**A** and **C**) and wild-type (**B** and **D**) hearts. (A and B) Intact heart cross-sections are shown. (C and D) IVS with part of right and LVs is shown. Morphometric analysis was applied to 4× images to measure the width of the IVS. The error bars present ±SE. *P*-value was determined by two-tailed *t*-test ($P = 0.01$). IVS, inter-ventricular septum; LV, left ventricle; RV, right ventricle. WT, $n = 4$; SMA, $n = 4$. Scale bar: 500 μm (A and B) and 200 μm (C and D).

prepared from the exact region of the heart in both groups demonstrate that septum remodeling in SMA mice leads to an enlargement of the LV at early (P5) and late time points (P9) (Figs 4 and 5). The area of the LV lumen was significantly larger in the SMA heart compared with wild-type at P9, providing further evidence of morphological defects shortly after birth (Supplementary Material, Fig. S1).

Arterial wall remodeling in the heart of SMAΔ7 mice

During our examination of P2 heart sections, we noticed arterial wall remodeling in SMA hearts. The arterial walls, veins and capillaries consist of a hollow center (lumen) through which the blood flows. The walls of both arteries and veins are composed of three layers: (i) adventitia (outer layer), (ii) media (intermediate layer) and (iii) intima (inner layer), but they differ in thickness. The media and intima layers of arteries are thicker than those of veins. This makes arteries more elastic and capable of expanding when blood surges through them from the beating heart. We have detected a considerably thinner arterial wall in SMA mice compared with the wild-type littermates ($P = 0.0002$) (Fig. 7). This phenotype cannot be explained by the smaller size of the SMA heart compared with

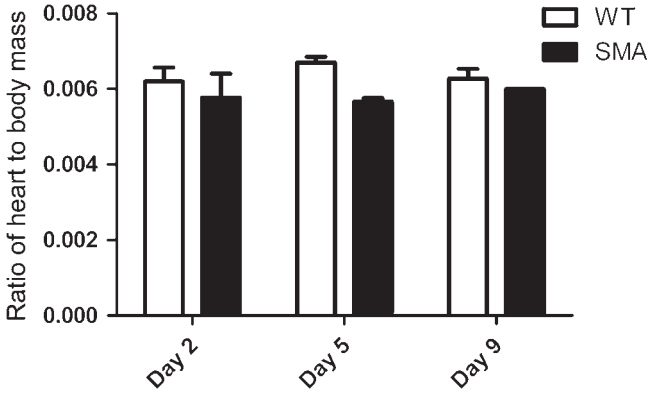

Figure 6. Cardiac hypertrophy does not occur in SMAΔ7 mice. The ratio of heart weight (g) to total body weight (g) was determined for SMAΔ7 and wild-type mice at indicated time points. The error bar represent ±SD. *P*-value was determined by one-way Anova ($P > 0.05$). WT, $n = 4$; SMA, $n = 4$.

wild-type since the size of their heart is almost identical at P2. It will be interesting to determine the specific layer of arteries that has been altered in thickness in the SMA heart and also the underlying mechanism that gives rise to its remodeling.

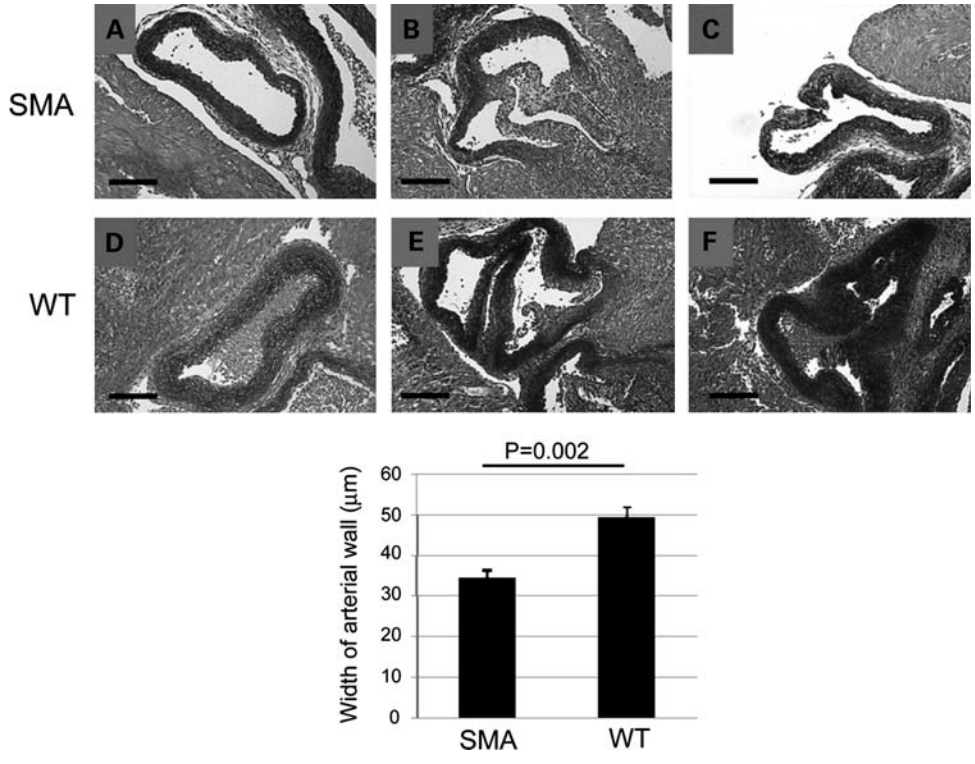

Figure 7. Arterial wall remodeling exists in 2-day-old hearts of SMAΔ7 mice. Representative bright-field images of 4 μm VVG-stained cross-sections of 2-day-old SMAΔ7 (**A**–**C**) and wild-type (**D**–**F**) hearts. Morphometric analysis was applied to 10× images to measure the width of the arterial wall. The error bars present ± SE. *P*-value was determined by two-tailed t test ($P = 0.0002$). WT, $n = 4$; SMA, $n = 4$. Scale bar: 100 μm.

Interstitial fibrosis begins in neonatal SMAΔ7 mice

Proliferation of interstitial fibroblasts and biosynthesis of extracellular matrix components in the heart are defined as cardiac fibrosis, which is a consequence of remodeling processes initiated by pathological events associated with a variety of cardiovascular disorders (19,20). This leads to abnormal myocardial stiffness and, ultimately, decreased cardiac function (21). We analyzed the bright-field images of VVG-stained heart sections for the deposition of collagen type III, an indicator of interstitial cardiac fibrosis, at P2, P5 and P9. VVG stains elastin (black), nuclei (blue black), collagen type III (pink) and connective tissue (yellow). Therefore, the intensity of the pink area was measured as an indicator of collagen deposition and interstitial fibrosis. Our results reveal that interstitial fibrosis has initiated modestly at P2 in SMAΔ7 mice (Fig. 8) and progresses rapidly as shown by the intensity of the pink area at P5 (Fig. 9). As expected, collagen deposition at P9 is more prevalent and significantly intensified compared with P5 (Figs 9 and 10). As anticipated, detectable collagen deposition is essentially absent in wild-type mice at each time point (Figs 8–10).

Oxidative stress is the underlying mechanism of cardiac fibrosis in SMAΔ7 mice

One of the underlying mechanisms for cardiac fibrosis is oxidative stress (22,23). Oxidative stress is caused by high levels of reactive oxygen species (ROS), which at low levels mediate antioxidant defenses and induce subtle changes in intracellular signaling pathways (redox signaling) (24). ROS are derived from many sources including mitochondria, xanthine oxidase, uncoupled nitric oxide synthases and NADPH oxidase (25,26). To test whether the observed cardiac fibrosis in SMAΔ7 mice is the result of excess ROS, we quantified the levels of the oxidative stress biomarkers in the heart. One of the most important biomarkers is angiotensin-II (Ang-II), which stimulates the activity of NADPH oxidase and plays a key role in cardiac remodeling (27–31). Previous work demonstrates that cardiac oxidative stress mediated by Ang-II promotes the development of cardiac fibrosis by upregulating TGF-beta1 expression, which subsequently enhances cardiac collagen synthesis and suppresses collagen degradation in hypertensive rats (23). All biological effects of Ang-II are mediated primarily by the AT1 receptor (AT1R) subtype (32). Therefore, we chose to quantify Ang-II and its receptor AT1R by immuno-histochemistry. To determine the involvement of NADPH oxidase in cardiac fibrosis, we quantified the levels of Nox2 and Rac1, which are two out of six subunits of NADPH oxidase (33). Analysis of confocal fluorescent images of P2 heart sections demonstrated that there is no significant difference in the levels of oxidative stress biomarkers between the SMA and wild-type mice (data not shown). The lack of oxidative stress at this stage correlates with a low level of fibrosis that is observed at P2. On the other hand, the levels of Nox2, Rac1 and Ang-II have increased slightly compared with the wild-type heart at P5 (Fig. 11). Interestingly, the level of AT1R has increased substantially in SMA mice at this time point (Fig. 11). As expected, the oxidative stress has progressed at P9 as our

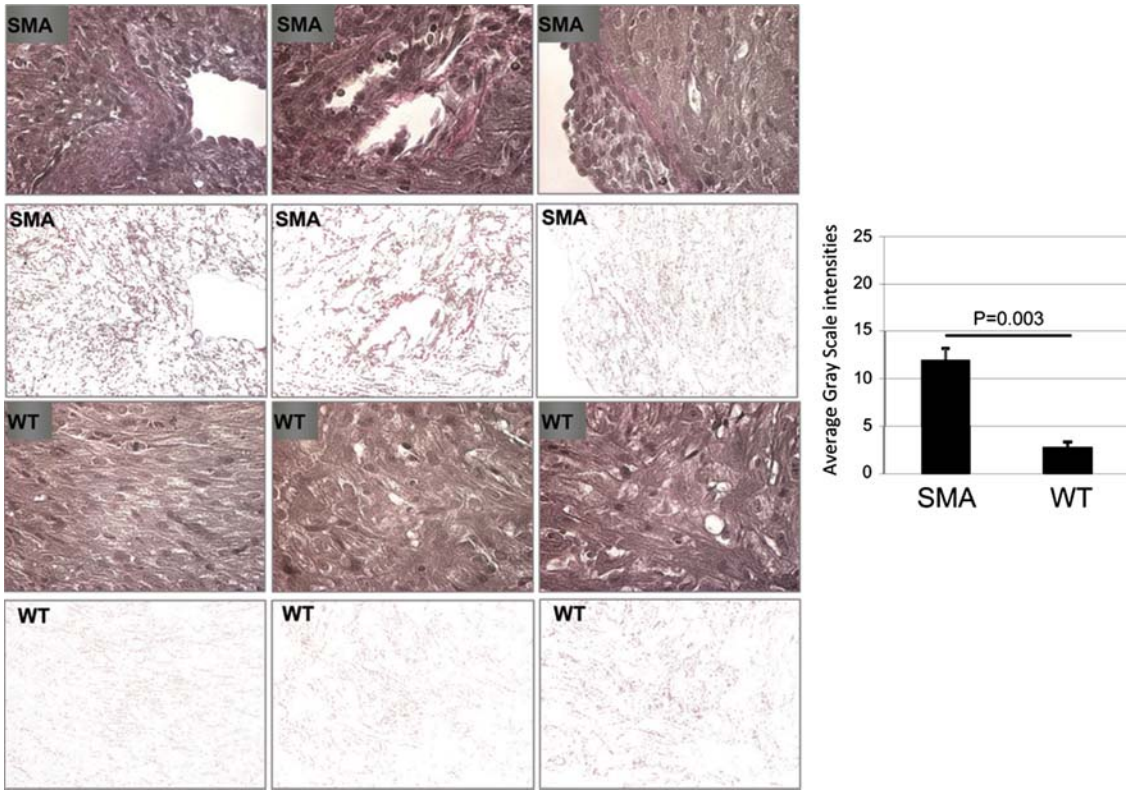

Figure 8. A low level of interstitial fibrosis exists in 2-day-old hearts of SMAΔ7 mice. Representative images of 4 μm VVG-stained cross-sections of hearts in 2-day-old SMAΔ7 and wild-type mice. VVG is specific for fibrosis and stains collagen type III (pink). In each animal group, the top row represents the bright-field images, whereas the bottom row only represents collagen staining. Morphometric analysis was applied to 40× images to discriminate collagen from elastin on the basis of the VVG staining. Collagen deposition is measured as gray-scale signal intensities that are represented as percentage of total area. The error bars present ± SE. *P*-value was determined by two-tailed *t*-test ($P = 0.003$). WT, $n = 4$; SMA, $n = 4$.

results demonstrate a significant increase in all of these proteins in the SMAΔ7 heart compared with wild-type (Fig. 12). These findings strongly suggest that the Ang-II-mediated oxidative stress contributes to cardiac fibrosis in SMAΔ7 mice.

SMAΔ7 mice has a slower heart rate than wild-type mice

The stiffness and lack of elasticity of cardio-myocytes that occur as a result of increased cardiac fibrosis at P9 will likely have a profound impact on cardiac function. We employed an electrocardiogram (ECG) to examine cardiac function in SMAΔ7 and wild-type mice at P9 to determine whether physiological functional differences existed. We used a modified version of the system previously described for recording ECGs in conscious mice without anesthesia or implants (34). The system includes three-lead, paw-sized conductive electrodes configured to record ECGs when three single electrodes contact three paws. Analysis of the signals demonstrated longer R–R intervals in SMA mice compared with wild-type mice (277 ± 27 versus 141 ± 28 ms, $P = 0.01$) (Fig. 13A), and consistent with the longer R–R intervals, significantly reduced heart rates were detected in SMAΔ7 mice compared with wild-type (221 ± 19 versus 464 ± 66 b.p.m., $P = 0.01$, $n = 4$) (Fig. 13B). Collectively, this work reveals structural and physiological defects in the hearts of SMA mouse models, which is consistent with defects in cardiac function at an early stage in disease development.

DISCUSSION

In severe SMA cases, a growing list of congenital heart defects are being recognized, including atrial septal defects, dilated RV, ventricular septal defects and hypoplastic left heart syndrome (15). Although the central nervous system and motor neurons are clearly central to any foreseeable therapeutic design for SMA, consideration of other cell types detectably affected by SMN deficiency will be a key to therapeutic success. That being the case, we have begun to examine cardiac tissue from SMA mouse models, and the goal of this research is to investigate the role of Smn in cardiac development and the impact it has on SMA phenotype and pathogenesis.

The most obvious cardiac remodeling revealed by histological analysis of heart cross-sections is septum thinning indicated by a significantly reduced IVS width. This defect initiates at embryonic stages in the severe model and between P3 and P5 in the SMAΔ7 model. Although this may be due to an undersized heart in SMA mice, there are reasons to suggest that this is not the primary determinant since we would also expect the area of the ventricles to be smaller in SMA mice compared with wild-type. Since our

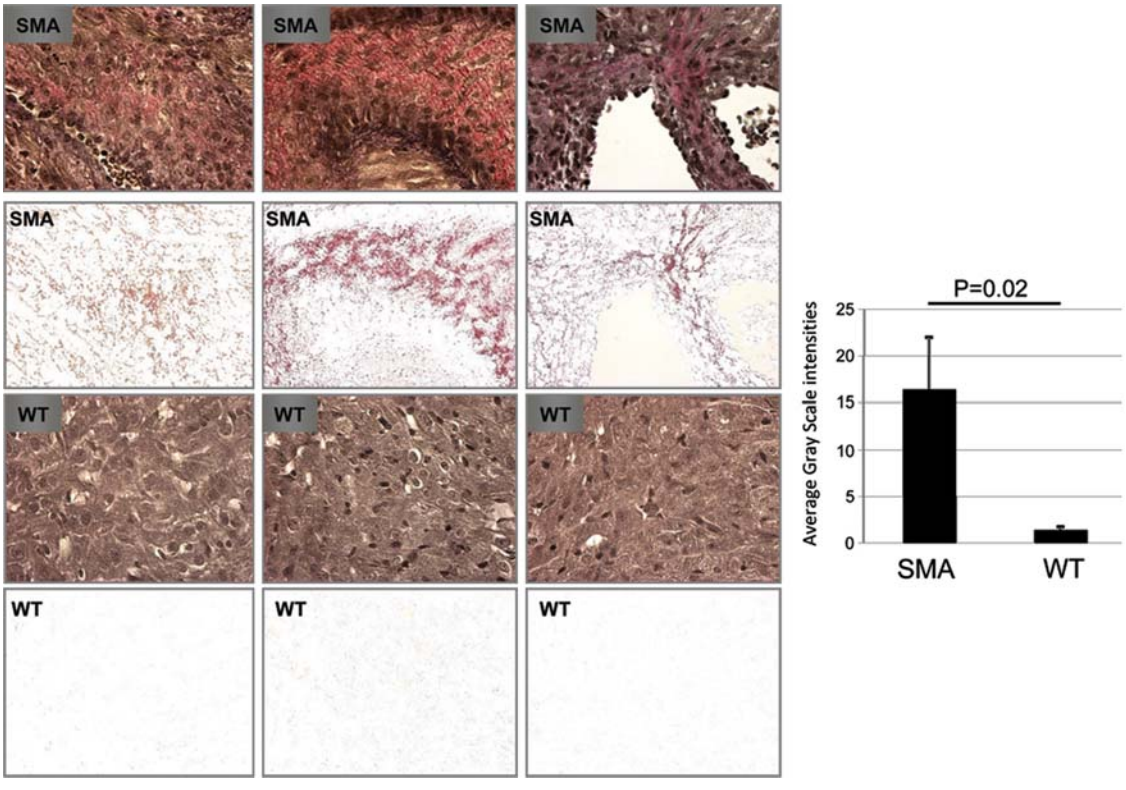

Figure 9. A moderate level of interstitial fibrosis exists in 5-day-old hearts of SMAΔ7 mice. Representative images of 4 μm VVG-stained cross-sections of hearts in 5-day-old SMAΔ7 and wild-type mice. VVG is specific for fibrosis and stains collagen type III (pink). In each animal group, the top row represents the bright-field images, whereas the bottom row only represents collagen staining. Morphometric analysis was applied to 40× images to discriminate collagen from elastin on the basis of the VVG staining. Collagen deposition is measured as gray-scale signal intensities that are represented as percentage of total area. The error bars present ±SE. *P*-value was determined by two-tailed *t*-test ($P = 0.02$). WT, $n = 4$; SMA, $n = 4$.

cross-sections are precisely prepared from the identical region of the heart in both animals, the observed enlargement of LV and even the RV at different time points is tightly associated with IVS remodeling. We are currently investigating the underlying mechanism of septum and LV wall thinning in both models of SMA mice by examining whether the cell division or reduced cell growth in these areas are responsible for remodeling.

Morphological observations also revealed partial loss of curvature in IVS of SMA mice. Previous reports have demonstrated that flattening of the IVS or D-shaped LV is correlated with the RV overload (35,36). RV overload is associated with chronic obstructive pulmonary diseases and atrial septal defects (36,37). Other signs of RV overload are RV enlargement and hypertrophy (38), which are detectable in the heart sections harvested at P9.

We examined the collagen type III deposition by quantifying the intensity of the pink area in VVG-stained heart sections harvested at different time points to determine the developmental phase at which the interstitial fibrosis initiates. Not surprisingly, we did not detect fibrosis at embryonic stages, since the lack of any strain or workload on the heart would not induce oxidative stress pathways. However, we observed interstitial fibrosis development in P2 SMAΔ7 mice, which became more advanced at each successive time point (P5 and P9). High levels of fibrosis at P9 were consistent with our functional analysis that demonstrated a much slower heart rate in P9 SMA mice. The source of cardiac fibrosis in the SMA heart was explored by testing the involvement of the renin–angiotensin system (RAS). Tissue-based RAS is known to modulate cell growth, differentiation, metabolism and tissue remodeling (39,40). RAS system is also involved in promoting oxidative stress-induced cardiac dysfunction (30,41). Enhanced RAS activity and oxidative stress have been demonstrated in several cardiovascular diseases, such as diabetes and hypertension (42,43), and are known to play a role in the pathogenesis of cardiac hypertrophy, remodeling, ventricular dysfunction and congestive heart failure (44–46). Ang-II is the main effector peptide in the RAS system that plays a role in proliferative, profibrotic and proinflammatory actions (27,47,48). In addition, accumulating evidence suggests that NADPH oxidases are major sources of ROS in the cardiovascular system (49–51). Nox2, a major subunit of NADPH oxidase, performs a critical role in Ang-II-induced cardiac fibrosis in that both NADPH oxidase activation and interstitial fibrosis were completely inhibited in $Nox2^{-/-}$ mice (52). Ang-II activates the Nox2 via the AT1R (29). Rac1 is a GTP-binding subunit of NADPH oxidase which plays a role by facilitating the interaction between NOX2 and other subunits and therefore activates the system (28,53). Thus, quantification of these proteins was a logical choice to examine the Ang-II-mediated oxidative stress through NADPH oxidase in

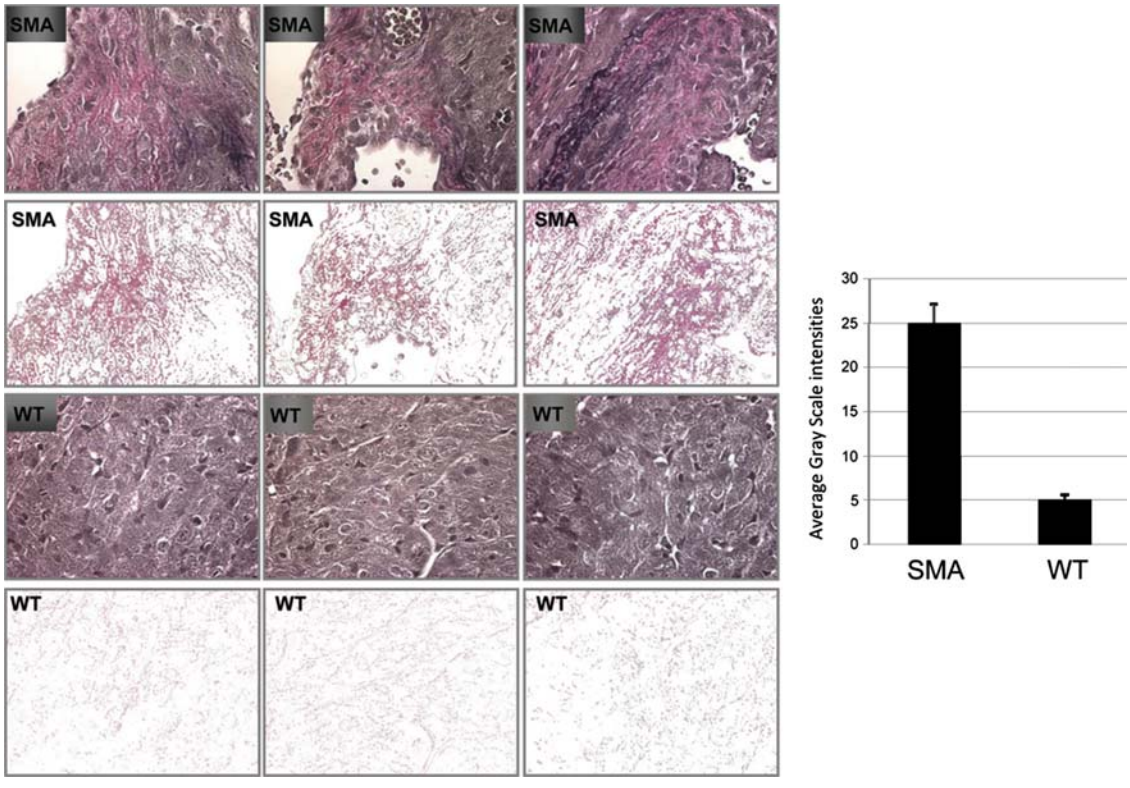

Figure 10. The level of interstitial fibrosis has intensified significantly in 9-day-old hearts of SMAΔ7 mice. Representative images of 4 μm VVG-stained cross-sections of hearts in 5-day-old SMAΔ7 and wild-type mice. VVG is specific for fibrosis and stains collagen type III (pink). In each animal group, the top row represents the bright-field images, whereas the bottom row only represents collagen staining. Morphometric analysis was applied to 40× images to discriminate collagen from elastin on the basis of the VVG staining. Collagen deposition is measured as gray-scale signal intensities that are represented as percentage of total area. The error bars present ±SE. *P*-value was determined by two-tailed *t*-test ($P = 0.02$). WT, $n = 4$; SMA, $n = 4$.

the SMA heart. The significant increase in the levels of all these proteins at P9 clearly indicates the involvement of RAS and NADPH oxidase in cardiac fibrosis of SMA mice.

Interestingly, the role of NADPH oxidase in accelerating the selective motor neuron degeneration in ALS mice has been previously described (54). Whether the increased expression of NADPH oxidase in SMA hearts is correlated with the level of this enzyme in the spinal cord remains to be seen. The fact that interstitial fibrosis at P5 was more prominent than P2, but the levels of oxidative stress proteins except AT1R were not markedly increased at this stage, suggests that additional oxidative stress pathways are contributing to cardiac fibrosis. The most interesting observation was the level of AT1R in P5 and P9 hearts, which was significantly higher than that in the wild-type heart. It has been well established that upregulated AT1R expression in the rostral ventrolateral medulla and its enhanced intracellular signaling transduction result in excessive sympathetic outflow to the heart, leading to chronic heart failure (55). The sympatho-excitation effect is due to an imbalance in expression levels of AT1R and AT2R, two receptors of Ang-II, with AT2R being downregulated significantly (55). It is critical to investigate the expression levels of these two proteins in the brain stem of SMA mice to determine whether a similar imbalance exists and contributes to cardiac defects. There is evidence that the compounds which inhibit the action of AT1R contain a cardio-protective effect and ameliorate myocardial remodeling and heart failure (56–60). It will be important to test the AT1R blockers in SMA mice and investigate its potential positive effects on the heart.

It is difficult to draw direct comparisons between the animal model and SMA patients; however, it is interesting to note the similarities regarding cardiac defects. In SMA patients, autonomic dysfunctions have been previously described, although primarily in type I patients (61–65). High levels of fibrosis and oxidative stress at P9 were associated with a much slower heart rate in the SMA mice. The pacemaker function of mammalian hearts is mediated by the sinoatrial node (SAN). SAN dysfunction leads to abnormally slow heart rates (bradycardia), leading to palpitations, fatigue and even syncope (66). The autonomic nervous system controls the decelerating and accelerating of spontaneous SAN activity through cholinergic and adrenergic stimulation. Several ionic currents contribute to cardiac automaticity and some of these currents are regulated by the autonomic nervous system (67–69). It will be important to investigate whether the physiology of the autonomic system is altered in the SMA models of disease as well.

Although it is not clear what specific SMN-associated function is linked to SMA development, it is clear that it is low levels of SMN that cause disease—not the ablation of SMN. It may be that in less severe forms of SMA, in which SMN

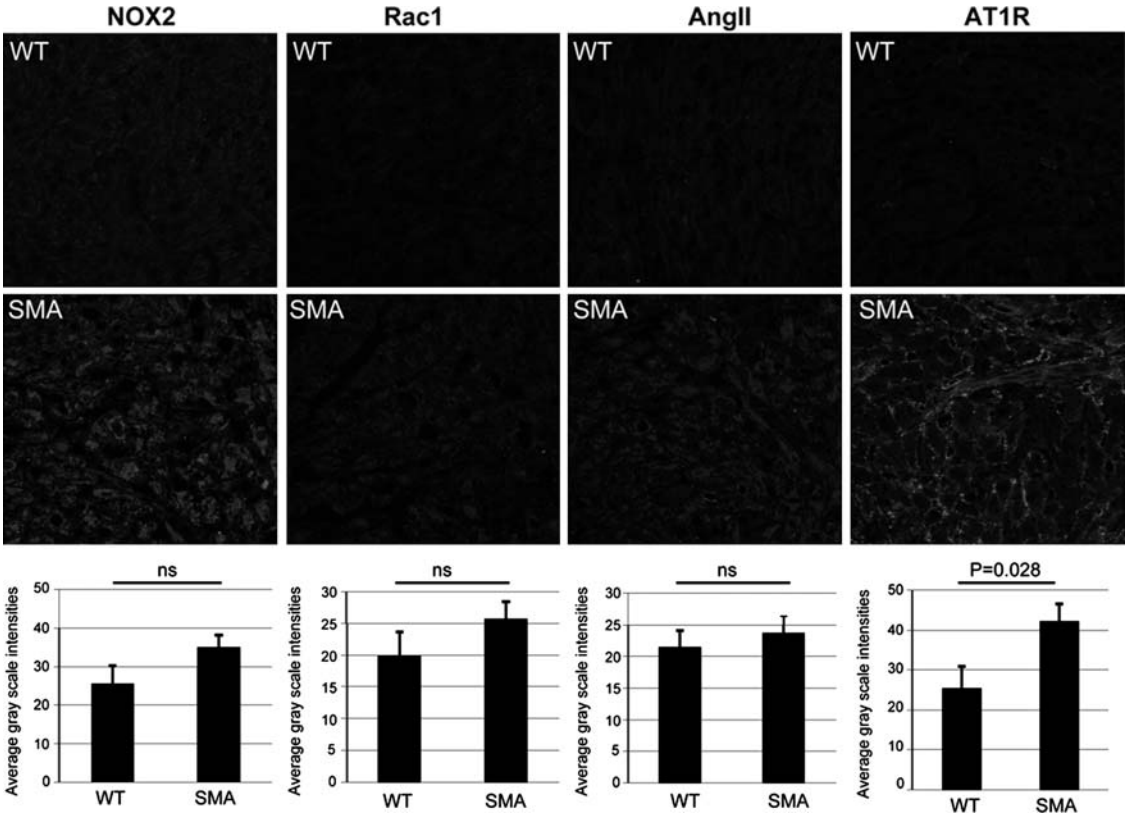

Figure 11. Oxidative stress is initiated at low levels in 5-day-old SMAΔ7 mice. Representative confocal images of LV cross-sections of 5-day-old SMAΔ7 and wild-type hearts immuno-stained for NADPH oxidase subunits (Nox2 and Rac1) and a member of RAS (Ang-II) and its receptor (AT1R). The expression level of each protein was measured by morphometric analysis as a gray-scale signal intensity. The error bars present $\pm$SE. *P*-value was determined by two-tailed *t*-test ($P > 0.05$ for Nox2, Rac1 and Ang-II; $P < 0.05$ for AT1R). WT, $n = 4$; SMA, $n = 4$.

levels are slightly higher, only the most sensitive tissues, such as motor neurons, are affected. However, as SMN levels drop dramatically lower, additional tissues are impacted. In this scenario, a critical SMN function such as snRNP assembly or axonal mRNA transport is disrupted in motor neurons at one threshold of SMN levels. However, if SMN levels are even lower as in type I patients or the severe mouse models, a more widespread pathology is observed. Since SMN is intricately involved in a general RNA pathway, snRNP assembly, this could help explain why more tissues are adversely affected in the most severe forms of disease.

The primary tissue affected in SMA are motor neurons with significant secondary effects exhibited in voluntary muscle groups following motor neuron degeneration. Congenital heart defects including septal defects and ventricular dysfunction have been documented in severe SMA cases, with hypoplastic left heart syndrome being the most commonly detected developmental defect. At this time, no cure exists for SMA, and approved therapies fail to provide meaningful cessation of degeneration or reversal of disease symptoms. Although the rescue of the central nervous system and motor neurons is clearly critical to any practical therapeutic design, detection of other cell types affected by SMN deficiency is a key to therapeutic success. In Duchenne muscular dystrophy, defects in skeletal muscle were the primary clinical concern. However, as supportive care advanced and patients lived longer, it became apparent that an underlying cardiac condition was also present that had not been fully appreciated previously (70). As SMA therapeutics and supportive measures progress further, it is essential to fully comprehend the role of SMN in cardiac development and to determine whether additional tissues are damaged in SMA patients other than motor neurons—especially in severe SMA cases. This is especially important as the SMA field moves forward toward increasing numbers of clinical trials. Our research has only begun to open a path toward recognizing the role of SMN in cardiac dysfunction, and a great deal of research is needed to understand the underlying pathways which participate in cardiac failure due to SMN deficiency.

MATERIALS AND METHODS

SMA animals

All animal experiments took place in accordance with procedures approved by the Animal Care and Use Committee (ACUC) of the University of Missouri. SMAΔ7 ($Smn^{-/-}$, $SMN2^{+/+}$, $SMN\Delta7^{+/+}$) animals were genotyped at the day of birth (day 1) as described previously (71). Following breeding of heterozygous mating partners ($Smn^{-/+}$, $SMN2^{+/+}$), the embryos were harvested at day 17.5 and the hearts were collected. The embryos were then genotyped to identify the

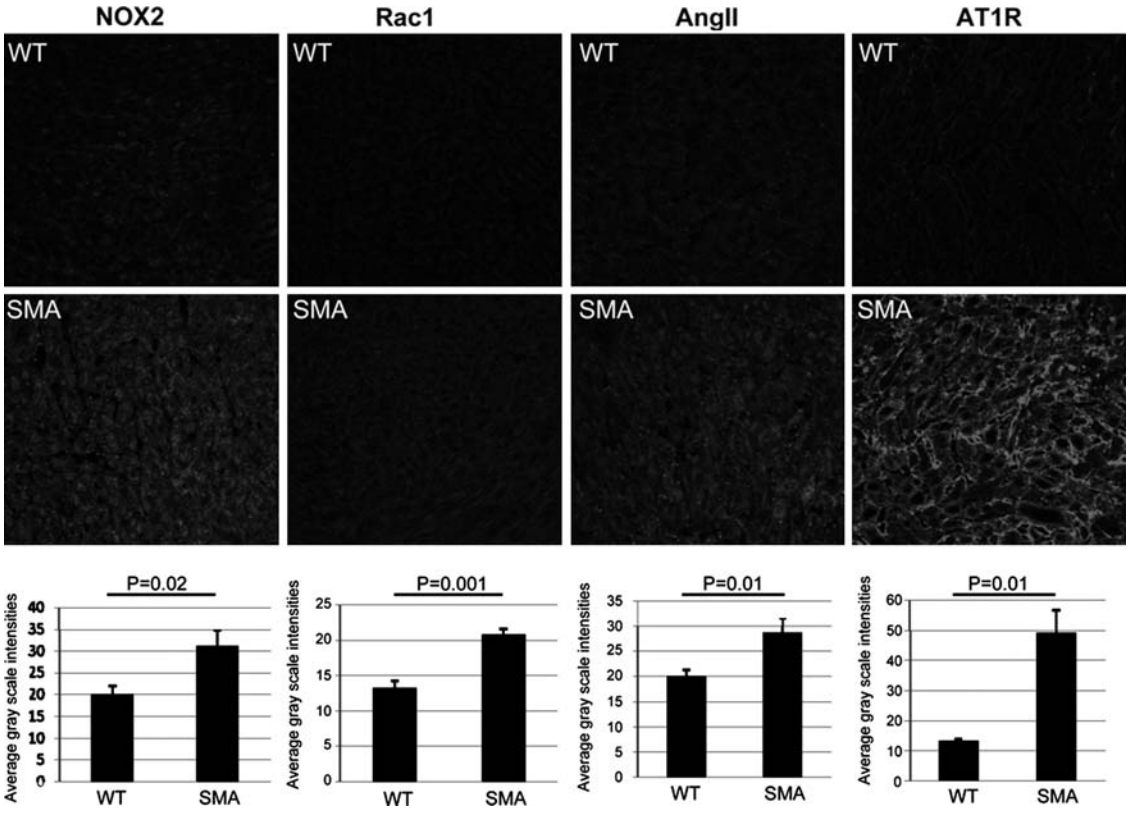

Figure 12. Oxidative stress biomarkers are expressed at high levels in 9-day-old SMAΔ7 mice. Representative confocal images of LV cross-sections of 9-day-old SMAΔ7 and wild-type hearts immuno-stained for NADPH oxidase subunits (Nox2 and Rac1) and a member of RAS (Ang-II) and its receptor (AT1R). The expression level of each protein was measured by morphometric analysis as a gray-scale signal intensity. The error bars present ± SE. *P*-value was determined by two-tailed *t*-test ($P < 0.05$ for Nox2, Rac1, Ang-II and AT1R). WT, $n = 4$; SMA, $n = 4$.

homozygous SMA knock out ($Smn^{-/-}$, $SMN2^{+/+}$) and wild-type ($Smn^{+/+}$, $SMN2^{+/+}$).

Quantification of remodeling in septum, left ventricular wall and arterial wall

The SMA and wild-type mice were handled according to ACUC regulations. Briefly, the animals were anesthetized with isoflurane (Vet One) and euthanized at selected time points, and the heart tissues from embryos and postnatal animals were collected, fixed in 4% paraformaldehyde and kept in 4°C. After 24 h fixation period, tissues were placed in histological cassettes and dehydrated with ethanol series, infiltrated with low-melting (50°C) paraplast and embedded in high-melting (56°C) paraplast. Then, the heart tissues were sectioned by 4 μm at 50 μm intervals. Four micrometer paraffin sections of heart tissue were stained with VVG, which stains elastin (black), nuclei (blue black), collagen (pink) and connective tissue (yellow). The slides were then analyzed with a Nikon50i microscope. Several images of IVS were captured for each slide with 4× magnification using a cool snap*cf* camera (Boyce Scientific Inc., Gray Summit, MO, USA). Using the same camera, several images for arteries and left ventricular wall were captured for each slide with 10× magnification. In order to determine the precise remodeling of arterial wall, the images of all existed arteries on the sections were captured. The thickness of septum, left ventricular wall and the arterial wall were precisely quantified by morphometric analysis using MetaVue and Metamorph software (Boyce Scientific Inc.).

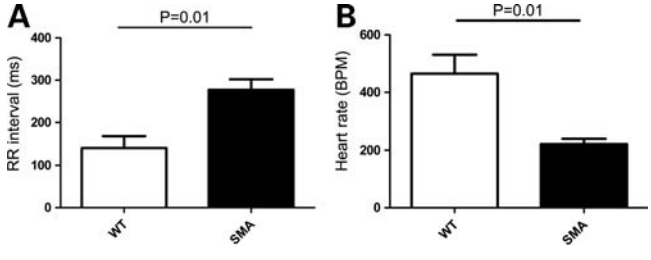

Figure 13. SMAΔ7 mice have a significantly slower heart rate than the wild-type mice. Three gel-coated ECG electrode lead systems were used to contact three paws in 9-day-old conscious SMAΔ7 and wild-type animals. (**A**) R–R intervals (ms) were recorded for at least 2 s for each lead to provide equivalent continuous recordings of 20–30 beats. (**B**) Heart rate (b.p.m.) was calculated with averaged R–R intervals in seconds divided by 60. Error bars represent ± SD. Two-paired *t*-test was used to compare the heart rate between two groups ($P = 0.01$). WT, $n = 4$; SMA, $n = 4$.

Quantification of interstitial fibrosis

The heart tissues were harvested at different time points, fixed and prepared as mentioned earlier. Four micrometer paraffin

sections of heart tissue were stained with VVG, which stains elastin (black), nuclei (blue black), collagen (pink) and connective tissue (yellow). The slides were then analyzed with a Nikon50i microscope and several images from different parts of the heart for each slide were captured with 40× magnification using a cool snap*cf* camera (Boyce Scientific Inc.). The signal intensities of the pink areas on each image which is indicative of the degree and level of interstitial fibrosis in heart tissue were quantified by MetaVue.

Quantification of NADPH oxidase subunits and RAS components

Immuno-histochemistry was used to quantify the expression level of Nox2, Rac1, Ang-II and AT1R as described previously (27,28). Briefly, harvested hearts were immersed and fixed in 4% paraformaldehyde. After 24 h fixation, tissues were placed in histological cassettes and dehydrated with ethanol series, infiltrated with low-melting (50°C) paraplast and embedded in high-melting (56°C) paraplast. Then, the heart tissues were sectioned by 4 μm at 50 μm intervals, the sections were deparaffinized in CitriSolv (Fisher Scientific) and rehydrated in ethanol series and HEPES wash buffer. Non-specific binding sites were blocked with donkey blocker (5% BSA, 5% of donkey serum and 0.01% sodium aside in HEPES buffer) for 4 h in a humidity chamber. Following a brief rinse, sections were incubated with primary antibodies: 1:100 goat polyclonal anti-Ang-II, 1:100 rabbit polyclonal anti -AT_1R, 1:100 goat polyclonal anti-Nox2 and 1:100 rabbit polyclonal anti-Rac1 (Santa Cruz Biotechnology, Santa Cruz, CA, USA) in a 10-fold diluted blocking agent overnight. After washing, the sections were incubated with 1:300 Alexa-fluor donkey anti-goat 647 (Invitrogen) for Ang-II and Nox2, and donkey anti-rabbit for AT1R and Rac1 (Invitrogen) for 4 h at room temperature. The slides were washed and mounted with Mowiol and stored in a light-tight slide box at 4°C until assessment. Using a bi-photon confocal microscope (Zeiss LSM, 510 MLO Thornwood, NY, USA), 1024 × 1024 pixel images were captured with LSM imaging system under the same computer settings for all sections in each experiment, and the signal intensities were analyzed with MetaVue software.

ECG recording

For ECG, we used a modified version of the previously described method (34). Briefly, three gel-coated ECG electrodes were used to contact three paws in conscious animals. The electrodes were connected to Spacelab model 90702 ECG recorder (Redmond, WA, USA) by a shielded three-electrode lead set. We used an adhesive tape across the upper abdomen to hold the mouse in the supine position. The animal usually struggled for <1 min and then limb movement was slowed down. ECG traces were recorded when the mouse movement had stopped. Three-electrode lead system closely contacted with left and right fore limbs and left hind limb following application of Spectra 360 ECG gel (Parker Laboratories, Inc., Fairfield, NJ, USA). The ECG traces were recorded when all three paws contacted the electrodes. Data were acquired at least 2 s for each lead to provide equivalent continuous recordings of 20–30 beats. Heart rate (b.p.m.) was calculated with averaged R–R interval in seconds divided by 60. Two-paired *t*-test was used to compare the heart rate between two groups.

SUPPLEMENTARY MATERIAL

Supplementary Material is available at *HMG* online.

ACKNOWLEDGEMENTS

We would like to thank John Marston and Erkan Osman for assistance with the mouse colony. We also thank Hansjorg Rindt for his valuable comments.

Conflict of Interest statement. None declared.

FUNDING

This work was supported by a grant from the University of Missouri College of Veterinary Medicine. M.S. is supported by SMA Europe.

REFERENCES

1. Pearn, J. (1980) Classification of spinal muscular atrophies. *Lancet*, **1**, 919–922.
2. Burnett, B.G., Crawford, T.O. and Sumner, C.J. (2009) Emerging treatment options for spinal muscular atrophy. *Curr. Treat. Options Neurol.*, **11**, 90–101.
3. Lefebvre, S., Burglen, L., Reboullet, S., Clermont, O., Burlet, P., Viollet, L., Benichou, B., Cruaud, C., Millasseau, P., Zeviani, M. *et al.* (1995) Identification and characterization of a spinal muscular atrophy-determining gene. *Cell*, **80**, 155–165.
4. Rochette, C.F., Gilbert, N. and Simard, L.R. (2001) SMN gene duplication and the emergence of the SMN2 gene occurred in distinct hominids: SMN2 is unique to *Homo sapiens*. *Hum. Genet.*, **108**, 255–266.
5. Lorson, C.L., Hahnen, E., Androphy, E.J. and Wirth, B. (1999) A single nucleotide in the SMN gene regulates splicing and is responsible for spinal muscular atrophy. *Proc. Natl Acad. Sci. USA*, **96**, 6307–6311.
6. Monani, U.R., Lorson, C.L., Parsons, D.W., Prior, T.W., Androphy, E.J., Burghes, A.H. and McPherson, J.D. (1999) A single nucleotide difference that alters splicing patterns distinguishes the SMA gene SMN1 from the copy gene SMN2. *Hum. Mol. Genet.*, **8**, 1177–1183.
7. Cartegni, L. and Krainer, A.R. (2002) Disruption of an SF2/ASF-dependent exonic splicing enhancer in SMN2 causes spinal muscular atrophy in the absence of SMN1. *Nat. Genet.*, **30**, 377–384.
8. Heier, C.R. and DiDonato, C.J. (2009) Translational readthrough by the aminoglycoside geneticin (G418) modulates SMN stability *in vitro* and improves motor function in SMA mice *in vivo*. *Hum. Mol. Genet.*, **18**, 1310–1322.
9. Lorson, C.L. and Androphy, E.J. (2000) An exonic enhancer is required for inclusion of an essential exon in the SMA-determining gene SMN. *Hum. Mol. Genet.*, **9**, 259–265.
10. Mattis, V.B., Bowerman, M., Kothary, R. and Lorson, C.L. (2008) A SMNDelta7 read-through product confers functionality to the SMNDelta7 protein. *Neurosci. Lett.*, **442**, 54–58.
11. Novelli, G., Semprini, S., Capon, F. and Dallapiccola, B. (1997) A possible role of NAIP gene deletions in sex-related spinal muscular atrophy phenotype variation. *Neurogenetics*, **1**, 29–30.
12. Burghes, A.H. and Beattie, C.E. (2009) Spinal muscular atrophy: why do low levels of survival motor neuron protein make motor neurons sick? *Nat. Rev. Neurosci.*, **10**, 597–609.
13. Gavrilina, T.O., McGovern, V.L., Workman, E., Crawford, T.O., Gogliotti, R.G., DiDonato, C.J., Monani, U.R., Morris, G.E. and Burghes, A.H. (2008) Neuronal SMN expression corrects spinal muscular atrophy

in severe SMA mice while muscle-specific SMN expression has no phenotypic effect. *Hum. Mol. Genet.*, **17**, 1063–1075.
14. Sohal, D.S., Nghiem, M., Crackower, M.A., Witt, S.A., Kimball, T.R., Tymitz, K.M., Penninger, J.M. and Molkentin, J.D. (2001) Temporally regulated and tissue-specific gene manipulations in the adult and embryonic heart using a tamoxifen-inducible Cre protein. *Circ. Res.*, **89**, 20–25.
15. Rudnik-Schoneborn, S., Heller, R., Berg, C., Betzler, C., Grimm, T., Eggermann, T., Eggermann, K., Wirth, R., Wirth, B. and Zerres, K. (2008) Congenital heart disease is a feature of severe infantile spinal muscular atrophy. *J. Med. Genet.*, **45**, 635–638.
16. Monani, U.R., Coovert, D.D. and Burghes, A.H. (2000) Animal models of spinal muscular atrophy. *Hum. Mol. Genet.*, **9**, 2451–2457.
17. Monani, U.R., Sendtner, M., Coovert, D.D., Parsons, D.W., Andreassi, C., Le, T.T., Jablonka, S., Schrank, B., Rossol, W., Prior, T.W. *et al.* (2000) The human centromeric survival motor neuron gene (SMN2) rescues embryonic lethality in Smn(−/−) mice and results in a mouse with spinal muscular atrophy. *Hum. Mol. Genet.*, **9**, 333–339.
18. Shiokawa, Y. and Becker, A.E. (1997) The left ventricular outflow tract in atrioventricular septal defect revisited: surgical considerations regarding preservation of aortic valve integrity in the perspective of anatomic observations. *J. Thorac. Cardiovasc. Surg.*, **114**, 586–593.
19. Akiyama-Uchida, Y., Ashizawa, N., Ohtsuru, A., Seto, S., Tsukazaki, T., Kikuchi, H., Yamashita, S. and Yano, K. (2002) Norepinephrine enhances fibrosis mediated by TGF-beta in cardiac fibroblasts. *Hypertension*, **40**, 148–154.
20. Samuel, C.S., Unemori, E.N., Mookerjee, I., Bathgate, R.A., Layfield, S.L., Mak, J., Tregear, G.W. and Du, X.J. (2004) Relaxin modulates cardiac fibroblast proliferation, differentiation, and collagen production and reverses cardiac fibrosis *in vivo*. *Endocrine*, **145**, 4125–4133.
21. Tamura, N., Ogawa, Y., Chusho, H., Nakamura, K., Nakao, K., Suda, M., Kasahara, M., Hashimoto, R., Katsuura, G., Mukoyama, M. *et al.* (2000) Cardiac fibrosis in mice lacking brain natriuretic peptide. *Proc. Natl Acad. Sci. USA*, **97**, 4239–4244.
22. Aragno, M., Mastrocola, R., Alloatti, G., Vercellinatto, I., Bardini, P., Geuna, S., Catalano, M.G., Danni, O. and Boccuzzi, G. (2008) Oxidative stress triggers cardiac fibrosis in the heart of diabetic rats. *Endocrine*, **149**, 380–388.
23. Zhao, W., Zhao, T., Chen, Y., Ahokas, R.A. and Sun, Y. (2008) Oxidative stress mediates cardiac fibrosis by enhancing transforming growth factor-beta1 in hypertensive rats. *Mol. Cell. Biochem.*, **317**, 43–50.
24. Soberman, R.J. (2003) The expanding network of redox signaling: new observations, complexities, and perspectives. *J. Clin. Invest.*, **111**, 571–574.
25. Saavedra, W.F., Paolocci, N., St John, M.E., Skaf, M.W., Stewart, G.C., Xie, J.S., Harrison, R.W., Zeichner, J., Mudrick, D., Marban, E. *et al.* (2002) Imbalance between xanthine oxidase and nitric oxide synthase signaling pathways underlies mechanoenergetic uncoupling in the failing heart. *Circ. Res.*, **90**, 297–304.
26. Satoh, M., Fujimoto, S., Haruna, Y., Arakawa, S., Horike, H., Komai, N., Sasaki, T., Tsujioka, K., Makino, H. and Kashihara, N. (2005) NAD(P)H oxidase and uncoupled nitric oxide synthase are major sources of glomerular superoxide in rats with experimental diabetic nephropathy. *Am. J. Physiol. Renal Physiol.*, **288**, F1144–F1152.
27. Habibi, J., Whaley-Connell, A., Qazi, M.A., Hayden, M.R., Cooper, S.A., Tramontano, A., Thyfault, J., Stump, C., Ferrario, C., Muniyappa, R. *et al.* (2007) Rosuvastatin, a 3-hydroxy-3-methylglutaryl coenzyme a reductase inhibitor, decreases cardiac oxidative stress and remodeling in Ren2 transgenic rats. *Endocrine*, **148**, 2181–2188.
28. Habibi, J., Whaley-Connell, A., Hayden, M.R., DeMarco, V.G., Schneider, R., Sowers, S.D., Karuparthi, P., Ferrario, C.M. and Sowers, J.R. (2008) Renin inhibition attenuates insulin resistance, oxidative stress, and pancreatic remodeling in the transgenic Ren2 rat. *Endocrine*, **149**, 5643–5653.
29. Whaley-Connell, A., Govindarajan, G., Habibi, J., Hayden, M.R., Cooper, S.A., Wei, Y., Ma, L., Qazi, M., Link, D., Karuparthi, P.R. *et al.* (2007) Angiotensin II-mediated oxidative stress promotes myocardial tissue remodeling in the transgenic (mRen2) 27 Ren2 rat. *Am. J. Physiol. Endocrinol. Metab.*, **293**, E355–E363.
30. Sowers, J.R. (2002) Hypertension, angiotensin II, and oxidative stress. *N. Engl. J. Med.*, **346**, 1999–2001.
31. Ritz, E. and Haxsen, V. (2003) Angiotensin II and oxidative stress: an unholy alliance. *J. Am. Soc. Nephrol.*, **14**, 2985–2987.
32. Berk, B.C. (2003) Angiotensin type 2 receptor (AT2R): a challenging twin. *Sci. STKE*, **2003**, PE16.
33. Li, Q., Harraz, M.M., Zhou, W., Zhang, L.N., Ding, W., Zhang, Y., Eggleston, T., Yeaman, C., Banfi, B. and Engelhardt, J.F. (2006) Nox2 and Rac1 regulate H2O2-dependent recruitment of TRAF6 to endosomal interleukin-1 receptor complexes. *Mol. Cell. Biol.*, **26**, 140–154.
34. Chu, V., Otero, J.M., Lopez, O., Morgan, J.P., Amende, I. and Hampton, T.G. (2001) Method for non-invasively recording electrocardiograms in conscious mice. *BMC Physiol.*, **1**, 6.
35. Moses, D.A. and Axel, L. (2004) Quantification of the curvature and shape of the interventricular septum. *Magn. Reson. Med.*, **52**, 154–163.
36. Movahed, M.R., Hepner, A., Lizotte, P. and Milne, N. (2005) Flattening of the interventricular septum (D-shaped left ventricle) in addition to high right ventricular tracer uptake and increased right ventricular volume found on gated SPECT studies strongly correlates with right ventricular overload. *J. Nucl. Cardiol.*, **12**, 428–434.
37. Teo, K.S., Dundon, B.K., Molaee, P., Williams, K.F., Carbone, A., Brown, M.A., Worthley, M.I., Disney, P.J., Sanders, P. and Worthley, S.G. (2008) Percutaneous closure of atrial septal defects leads to normalisation of atrial and ventricular volumes. *J. Cardiovasc. Magn. Reson.*, **10**, 55.
38. Kato, S., Koide, M., Cooper, G. and Zile, M.R. (1996) Effects of pressure- or volume-overload hypertrophy on passive stiffness in isolated adult cardiac muscle cells. *Am. J. Physiol.*, **271**, H2575–H2583.
39. Sadoshima, J. and Izumo, S. (1993) Molecular characterization of angiotensin II-induced hypertrophy of cardiac myocytes and hyperplasia of cardiac fibroblasts. Critical role of the AT1 receptor subtype. *Circ. Res.*, **73**, 413–423.
40. Crabos, M., Roth, M., Hahn, A.W. and Erne, P. (1994) Characterization of angiotensin II receptors in cultured adult rat cardiac fibroblasts. Coupling to signaling systems and gene expression. *J. Clin. Invest.*, **93**, 2372–2378.
41. Grote, K., Drexler, H. and Schieffer, B. (2004) Renin–angiotensin system and atherosclerosis. *Nephrol. Dial. Transplant.*, **19**, 770–773.
42. Lastra-Lastra, G., Sowers, J.R., Restrepo-Erazo, K., Manrique-Acevedo, C. and Lastra-Gonzalez, G. (2009) Role of aldosterone and angiotensin II in insulin resistance: an update. *Clin. Endocrinol.*, **71**, 1–6.
43. Nistala, R., Wei, Y., Sowers, J.R. and Whaley-Connell, A. (2009) Renin–angiotensin–aldosterone system-mediated redox effects in chronic kidney disease. *Transl. Res.*, **153**, 102–113.
44. Werner, C.M. and Bohm, M. (2008) The therapeutic role of RAS blockade in chronic heart failure. *Ther. Adv. Cardiovasc. Dis.*, **2**, 167–177.
45. Sussman, M.A., Welch, S., Walker, A., Klevitsky, R., Hewett, T.E., Price, R.L., Schaefer, E. and Yager, K. (2000) Altered focal adhesion regulation correlates with cardiomyopathy in mice expressing constitutively active rac1. *J. Clin. Invest.*, **105**, 875–886.
46. Bendall, J.K., Cave, A.C., Heymes, C., Gall, N. and Shah, A.M. (2002) Pivotal role of a gp91(phox)-containing NADPH oxidase in angiotensin II-induced cardiac hypertrophy in mice. *Circulation*, **105**, 293–296.
47. Ferrario, C.M. and Strawn, W.B. (2006) Role of the renin–angiotensin–aldosterone system and proinflammatory mediators in cardiovascular disease. *Am. J. Cardiol.*, **98**, 121–128.
48. Marchesi, C., Paradis, P. and Schiffrin, E.L. (2008) Role of the renin–angiotensin system in vascular inflammation. *Trends Pharmacol. Sci.*, **29**, 367–374.
49. Dworakowski, R., Anilkumar, N., Zhang, M. and Shah, A.M. (2006) Redox signalling involving NADPH oxidase-derived reactive oxygen species. *Biochem. Soc. Trans.*, **34**, 960–964.
50. Lund, A.K., Peterson, S.L., Timmins, G.S. and Walker, M.K. (2005) Endothelin-1-mediated increase in reactive oxygen species and NADPH oxidase activity in hearts of aryl hydrocarbon receptor (AhR) null mice. *Toxicol. Sci.*, **88**, 265–273.
51. Hu, T., Ramachandrarao, S.P., Siva, S., Valancius, C., Zhu, Y., Mahadev, K., Toh, I., Goldstein, B.J., Woolkalis, M. and Sharma, K. (2005) Reactive oxygen species production via NADPH oxidase mediates TGF-beta-induced cytoskeletal alterations in endothelial cells. *Am. J. Physiol. Renal Physiol.*, **289**, F816–F825.
52. Johar, S., Cave, A.C., Narayanapanicker, A., Grieve, D.J. and Shah, A.M. (2006) Aldosterone mediates angiotensin II-induced interstitial cardiac fibrosis via a Nox2-containing NADPH oxidase. *FASEB J.*, **20**, 1546–1548.
53. Khanna, A.K. and Pieper, G.M. (2007) NADPH oxidase subunits (NOX-1, p22phox, Rac-1) and tacrolimus-induced nephrotoxicity in a rat renal transplant model. *Nephrol. Dial. Transplant.*, **22**, 376–385.

54. Wu, D.C., Re, D.B., Nagai, M., Ischiropoulos, H. and Przedborski, S. (2006) The inflammatory NADPH oxidase enzyme modulates motor neuron degeneration in amyotrophic lateral sclerosis mice. *Proc. Natl Acad. Sci. USA*, **103**, 12132–12137.
55. Gao, L., Wang, W.Z., Wang, W. and Zucker, I.H. (2008) Imbalance of angiotensin type 1 receptor and angiotensin II type 2 receptor in the rostral ventrolateral medulla: potential mechanism for sympathetic overactivity in heart failure. *Hypertension*, **52**, 708–714.
56. Privratsky, J.R., Wold, L.E., Sowers, J.R., Quinn, M.T. and Ren, J. (2003) AT1 blockade prevents glucose-induced cardiac dysfunction in ventricular myocytes: role of the AT1 receptor and NADPH oxidase. *Hypertension*, **42**, 206–212.
57. Jugdutt, B.I., Xu, Y., Balghith, M., Moudgil, R. and Menon, V. (2000) Cardioprotection induced by AT1R blockade after reperfused myocardial infarction: association with regional increase in AT2R, IP3R and PKCepsilon proteins and cGMP. *J. Cardiovasc. Pharmacol. Ther.*, **5**, 301–311.
58. Moudgil, R., Musat-Marcu, S., Xu, Y., Kumar, D. and Jugdutt, B.I. (2002) Increased AT2R protein expression but not increased apoptosis during cardioprotection induced by AT1R blockade. *Can. J. Cardiol.*, **18**, 873–883.
59. Baumann, M., Sollinger, D., Roos, M., Lutz, J. and Heemann, U. (2010) Prehypertensive preconditioning improves adult antihypertensive and cardioprotective treatment. *J. Pharmacol. Exp. Ther.*, **332**, 1121–1126.
60. Whaley-Connell, A., Habibi, J., Cooper, S.A., Demarco, V.G., Hayden, M.R., Stump, C.S., Link, D., Ferrario, C.M. and Sowers, J.R. (2008) Effect of renin inhibition and AT1R blockade on myocardial remodeling in the transgenic Ren2 rat. *Am. J. Physiol. Endocrinol. Metab.*, **295**, E103–E109.
61. Araujo Ade, Q., Araujo, M. and Swoboda, K.J. (2009) Vascular perfusion abnormalities in infants with spinal muscular atrophy. *J. Pediatr.*, **155**, 292–294.
62. Bach, J.R. (2007) Medical considerations of long-term survival of Werdnig–Hoffmann disease. *Am. J. Phys. Med. Rehabil.*, **86**, 349–355.
63. Finsterer, J. and Stollberger, C. (1999) Cardiac involvement in Werdnig–Hoffmann's spinal muscular atrophy. *Cardiology*, **92**, 178–182.
64. Hachiya, Y., Arai, H., Hayashi, M., Kumada, S., Furushima, W., Ohtsuka, E., Ito, Y., Uchiyama, A. and Kurata, K. (2005) Autonomic dysfunction in cases of spinal muscular atrophy type 1 with long survival. *Brain Dev.*, **27**, 574–578.
65. Huang, J.J., Jong, Y.J., Huang, M.Y., Chiang, C.H. and Huang, T.Y. (1996) Electrocardiographic findings in children with spinal muscular atrophy. *Jpn Heart J.*, **37**, 239–242.
66. Lamas, G.A., Lee, K., Sweeney, M., Leon, A., Yee, R., Ellenbogen, K., Greer, S., Wilber, D., Silverman, R., Marinchak, R. *et al.* (2000) The mode selection trial (MOST) in sinus node dysfunction: design, rationale, and baseline characteristics of the first 1000 patients. *Am. Heart J.*, **140**, 541–551.
67. Maltsev, V.A. and Lakatta, E.G. (2008) Dynamic interactions of an intracellular Ca2+ clock and membrane ion channel clock underlie robust initiation and regulation of cardiac pacemaker function. *Cardiovasc. Res.*, **77**, 274–284.
68. Maltsev, V.A., Vinogradova, T.M. and Lakatta, E.G. (2006) The emergence of a general theory of the initiation and strength of the heartbeat. *J. Pharmacol. Sci.*, **100**, 338–369.
69. Mangoni, M.E. and Nargeot, J. (2008) Genesis and regulation of the heart automaticity. *Physiol. Rev.*, **88**, 919–982.
70. Duan, D. (2006) Challenges and opportunities in dystrophin-deficient cardiomyopathy gene therapy. *Hum. Mol. Genet.*, **15 (Spec no. 2)**, R253–R261.
71. Coady, T.H., Baughan, T.D., Shababi, M., Passini, M.A. and Lorson, C.L. (2008) Development of a single vector system that enhances trans-splicing of SMN2 transcripts. *PLoS ONE*, **3**, e3468.